Electromechanical Modelling and Vibration Control Analysis of Cyclic Symmetric Structures with Piezoelectric Vibration Absorber

Yucai Zhong[a,b], Xinxing Ma[a,b], Jie Yuan[c] and Zhenguo Zhang[a,b,*]

[a]*State Key Laboratory of Mechanical System and Vibration, Shanghai Jiao Tong University, Shanghai 200240, China*

[b]*Institute of Vibration, Shock & Noise, Shanghai Jiao Tong University, Shanghai 200240, China*

[c]*Computational engineering design group, Department of aeronautics and astronautics, University of Southampton, SO16 3AY Southampton, UK*

Abstract

This study explored the application of piezoelectric vibration absorbers (PVAs) equipped with synthetic circuits for the vibration control of cyclic symmetric structures. A cyclic symmetric electromechanical model (CSEM) integrated with PVAs was introduced to facilitate the design and optimization of the PVAs. This model was formulated analytically based on the circulant matrix theory, and the dynamic response was computed using the complex mode superposition method with explicit consideration of the intrinsic resistance within the PVA. A case study involving a simplified blisk model and an experimental test rig was conducted to validate the proposed CSEM. The validity of the model was confirmed through a comparative analysis of both the natural and dynamic characteristics obtained using the finite element model and experimental results. Furthermore, the impact of synthetic circuit parameters (inductance and negative capacitance values) and the placement of piezoelectric patches on the vibration control performance of PVA were investigated. The results suggested that the optimal inductance coincide with the analytical value, whereas the optimal negative capacitance of the series was slightly greater than the intrinsic capacitance of the patch. Additionally, mounting the piezoelectric patch on the blade root improved the vibration control.

Keywords: Vibration control, electromechanical coupling, cyclic symmetric modelling, piezoelectric vibration absorber, blisk structure.

*Corresponding author. School of Mechanical Engineering, Shanghai Jiao Tong University, Shanghai 200240, China
E-mail addresses: zhongyucai@sjtu.edu.cn (Y. Zhong); xinxingma@sjtu.edu.cn (X. Ma); j.yuan@soton.ac.uk (J. Yuan); zzgjtx@sjtu.edu.cn (Z. Zhang)

1. Introduction

Cyclic symmetric structures serve as the critical components in numerous rotating machines, including compressors (Yang et al., 2022), turbines (Bladh et al., 2000; Zhou et al., 2014), and helicopter engines (Anusonti-Inthra and Gandhi, 2000). These structures, engineered for high-pressure and high-speed conditions, are prone to vibrations that may lead to high-cycle fatigue or substantial plastic deformation. Current control strategies primarily involve the implementation of damping technologies such as dry friction (Sun et al., 2021), constrained layer (Sun et al., 2020), and active control damping (Liu et al., 2017), which effectively attenuate peak dynamic responses to ensure operational safety (Ewins, 2010). Furthermore, the integration of piezoelectric vibration absorbers (PVAs) has been explored to enhance the vibration control in these structures.

PVAs have attracted considerable attention owing to their excellent properties, such as lightweight construction, broad operational bandwidths and ease of integration (Richardt et al., 2024; Soltani et al., 2014). Typically, PVAs incorporate a piezoelectric transducer with an electrical impedance (Berardengo et al., 2020; Gripp and Rade, 2018; Yamada et al., 2010). The RL resonant shunt circuit, comprising an inductor (L) and a resistor (R), is most commonly employed in PVAs (Soltani et al., 2014). PVAs have been successfully applied to various structures such as beams (Qi et al., 2023; Thomas et al., 2009), shells (Dai et al., 2023; Jamshidi and Jafari, 2022) and plates (Zhou et al., 2021), demonstrating effective vibration control. For cyclic symmetric structures, Cross and Fleeter (2002) explored the application of PVAs in turbomachine blades through a series of experiments. Tang and Wang (2003) demonstrated the effectiveness of PVA in eliminating the vibration localisation in cyclic symmetric structures owning to minor mistuning. Additional applications include helicopter rotors (Shevtsov et al., 2009) and circular saws (Pohl and Rose, 2016). These instances suggest that the application of PVAs to cyclic symmetric structures is likely to yield significant vibration reduction benefits.

Although traditional RL shunt circuits are effective, their scalability is constrained by the considerable inductance required to achieve resonance (Fleming et al., 2000; Shen et al., 2023). Several researchers have introduced synthetic circuits to enhance the vibration control capabilities of shunt circuits and simplify the construction of PVAs (Alfahmi and Erturk, 2024; Fleming et al., 2000; Luo et al., 2024). Synthetic RLNC shunt circuits, with negative capacitances (NCs) have proven to be highly effective for vibration control (Berardengo et al., 2021). Numerous studies have been conducted on the effect of NC on vibration control in PVAs applied to simple structures (Mosquera-Sánchez et al., 2024; Neubauer et al., 2006). For instance, Berardengo et al., (2016, 2021) provided practical guidelines and an analytical formula for NC implementation, with experimental evidence confirming its vibration damping benefits. However, the application of NC to cyclic symmetric structures has received less attention in literature.

To optimise the design of PVAs with synthetic circuits for cyclic symmetric structures, it is essential to develop a robust electromechanical model of cyclic symmetric structures integrated with PVAs. As reported in the literature, the lumped-parameter modelling method (Liu et al., 2017; Zhou et al., 2014) is widely used to create electromechanical models of cyclic symmetric structures with PVAs. Although this method effectively captures the vibration features, its simplified approach limits its utility in designing PVAs for cyclic symmetric structures. Recently, Shen et al. (2023) introduced a semi-analytical dynamic modelling approach for blisk structures with PVAs, exploring the optimal parameters for resistance and RL series circuits. Despite offering insights into the design of PVA in cyclic symmetric structures, this

method may fall short of precisely portraying the complex cyclic symmetric structures encountered in practical scenarios.

Cyclic symmetric structures lead to block-circulant dynamic matrices in the finite element method (FEM) (Olson et al., 2014; Pourkiaee et al., 2022). This characteristic allows for the decomposition of cyclic symmetric systems into a set of uncoupled systems through appropriate coordinate transformations. Early studies on cyclic symmetric structures focussed on the modes of vibration (Ewins, 1973) and the steady-state response under harmonic excitation (Ewins, 2010; Yuan et al., 2017) of turbomachinery. Bladh et al. (2000) established a cyclic symmetric model of the bladed disk and appleied the component mode synthesis techniques to reduce the computational effort. Petrov (2004) developed an effective method based on the cyclic symmetric theory to calculate the nonlinear dynamic response of blade disk. Pourkiaee et al. (2022) presented a novel reduced-order modelling technique for the nonlinear dynamics of mistuned bladed disks with friction interfaces. These studies underscore the significant computational savings achieved when cyclic symmetric is exploited. However, current studies have primarily addressed the mechanical aspects of cyclic symmetric structures, highlighting the lack of methods for modelling electromechanical systems with PVAs. This gap underscores the need for research that integrates the mechanical and electrical domains to develop more effective vibration control strategies.

In this study, a cyclic symmetric electromechanical model (CSEM) is proposed to evaluate the vibration characteristics of cyclic symmetric structures with PVA. The key contributions of this study are as follow: (1) A general and accurate electromechanical model for cyclic symmetric structures with PVAs was developed by integrating the complex mode superposition method to simulate dynamic responses. (2) A PVA with a synthetic circuit, including a negative capacitor, was designed to control the vibration of the cyclic symmetric structures. (3) A case study on a simplified blisk equipped with PVAs was conducted, involving numerical validation through FEM and experimental verification of the vibration control performance using a dedicated test rig.

This paper is organised as follows. In Section 2, an electromechanical modelling method for cyclic symmetric structures with PVAs is introduced, and the dynamic response of the electromechanical system is derived. In Section 3, the verification of the proposed model is verified by comparing the natural characteristics and vibration responses with the FEM and experiments. in Section 4, the effects of the circuit parameters and placement of the piezoelectric patch on the vibration control performance of PVA are investigated in Section 4, respectively. The conclusions are summarised in the last section.

2. Formulation of electromechanical modelling

Cyclic symmetric systems have block-circulant dynamic matrices. A notable characteristic of these matrices is their ability to be pseudo-diagonalized using real quasi-equivalent block Fourier matrices. In this section the CSEM method is formulated by analysing a cyclic symmetric structure equipped with PVA. Furthermore, a vibration analysis method that integrates CSEM with the complex mode superposition method is presented.

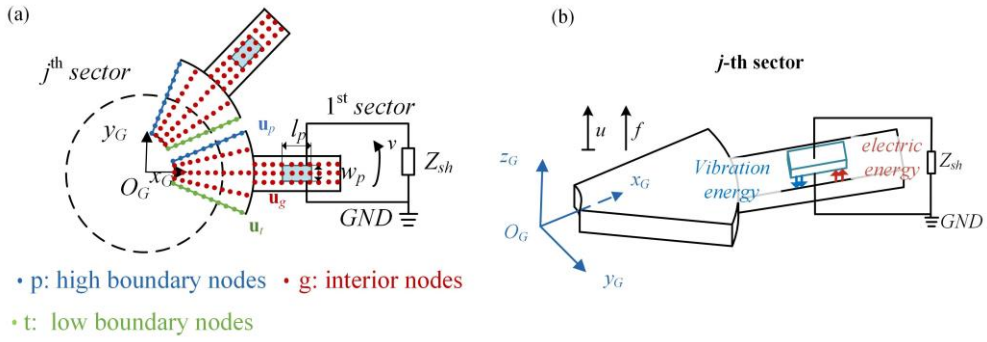

Figure 1. Model of the cyclic symmetric structure with PVA labelled with coordinate system: (a) Entire model; (b) the j-th sector of the system.

2.1. Electromechanical model of single sector

As illustrated in Figure 1, the model exhibits a typical cyclically symmetric structure when each sector is uniformly attached to an identical piezoelectric patch. The FEM of one sector attached to the piezoelectric patch is established as follows:

$$\begin{bmatrix} \mathbf{m}_{uu}^{j} & \mathbf{0} \\ \mathbf{0} & 0 \end{bmatrix} \begin{bmatrix} \ddot{\mathbf{u}}^{j} \\ \ddot{v}^{j} \end{bmatrix} + \begin{bmatrix} \mathbf{c}_{uu}^{j} & \mathbf{0} \\ \mathbf{0} & 0 \end{bmatrix} \begin{bmatrix} \dot{\mathbf{u}}^{j} \\ \dot{v}^{j} \end{bmatrix} + \begin{bmatrix} \mathbf{k}_{uu}^{j} & \mathbf{k}_{uv}^{j} \\ \mathbf{k}_{vu}^{j} & -k_{vv}^{j} \end{bmatrix} \begin{bmatrix} \mathbf{u}^{j} \\ v^{j} \end{bmatrix} = \begin{bmatrix} \mathbf{f}^{j} \\ q^{j} \end{bmatrix} \tag{1}$$

where $\mathbf{u}^j$, v^j and q^j are the nodal DOFs, denoting the displacement, voltage, and charge generated from the patch, respectively, and j denotes the index number. $\mathbf{m}_{uu}^{j}$, $\boldsymbol{c}_{uu}^{j}$ and $\mathbf{k}_{uu}^{j}$ denote the structure mass and stiffness matrices, respectively; the piezoelectric stiffness matrix $\mathbf{k}_{uv}^{j} = \mathbf{k}_{vu}^{j^T}$ couples the structural and electric behaviour, and k_{vv}^{j} is the dielectric stiffness matrix. Because electrical variables are used, this equation is convenient for introducing realistic electrical boundaries.

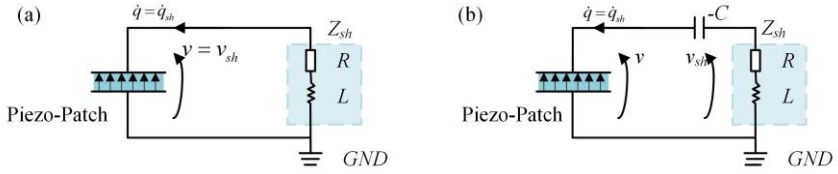

Figure 2. Piezoelectric patch with different shunt circuit: (a) series RL without NC (b) series RL with NC

In this study, two circuit layouts, as shown in Figure 2, were investigated using a CSEM. Considering that every sector in an electromechanical system is connected to a series circuit as shown in Figure 2(a), the relationship between q and v is as follows (Berardengo et al., 2016; Thomas et al., 2009).

$$L\ddot{q}^{j} + R\dot{q}^{j} - v^{j} = 0 \tag{2}$$

where L and R represent inductance and resistance respectively. By substituting voltage v^j into Eq. (1), the second line can be rewritten as follows.

$$L\ddot{q}^{j} + R\dot{q}^{j} + k_{vv}^{-1}q^{j} - k_{vv}^{-1}k_{vu}\mathbf{u}^{j} = 0 \tag{3}$$

Thus, the FEM of a single sector with a series RL shunt circuit is obtained as follows.

$$\begin{bmatrix} \mathbf{m}_{uu}^{j} & \mathbf{0} \\ \mathbf{0} & L \end{bmatrix} \begin{bmatrix} \ddot{\mathbf{u}}^{j} \\ \ddot{q}^{j} \end{bmatrix} + \begin{bmatrix} \mathbf{c}_{uu}^{j} & \mathbf{0} \\ \mathbf{0} & R \end{bmatrix} \begin{bmatrix} \dot{\mathbf{u}}^{j} \\ \dot{q}^{j} \end{bmatrix} + \begin{bmatrix} \tilde{\mathbf{k}}_{uu}^{j} & \tilde{\mathbf{k}}_{uv}^{j} \\ \tilde{\mathbf{k}}_{vu}^{j} & k_{vv}^{j} \end{bmatrix} \begin{bmatrix} \mathbf{u}^{j} \\ q^{j} \end{bmatrix} = \begin{bmatrix} \mathbf{f}^{j} \\ 0 \end{bmatrix} \tag{4}$$

$$\tilde{\mathbf{k}}_{uu}^{j} = \mathbf{k}_{uu}^{j} + \mathbf{k}_{uv}^{j}\left(k_{vv}^{j}\right)^{-1}\mathbf{k}_{vu}^{j}, \quad \tilde{k}_{vv}^{j} = \left(k_{vv}^{j}\right)^{-1}, \quad \tilde{\mathbf{k}}_{uv}^{j} = -\mathbf{k}_{uv}^{j}\left(k_{vv}^{j}\right)^{-1}, \quad \tilde{\mathbf{k}}_{vu}^{j} = \left(\tilde{\mathbf{k}}_{uv}^{j}\right)^{T} \tag{5}$$

When the NC is added to the circuit, as shown in Figure 2(b), the relationship between q and v becomes (Berardengo et al., 2021; Zhou and Hu, 2023):

$$L\ddot{q}^j + R\dot{q}^j + \frac{1}{C_{neg}} q^j - v^j = 0 \tag{6}$$

The electromechanical model has the same form as that in (4), with the following exception:

$$\tilde{k}_{vv}^j = \left(k_{vv}^j\right)^{-1} + 1/C_{neg} \tag{7}$$

where C_{neg} represents the NC value. The shunt circuit parameters must be tuned for specific-mode vibration control. The tuned formulations are presented in the Appendix.

2.2. Cycle symmetric electromechanical model (CSEM) and vibration analysis

Subsequently, by assembling the structural matrices of each sector in sequence, the resulting matrices for the cyclic symmetric structure take the form of circulant matrices. A block circulant dynamics matrix with generating elements $\mathbf{C}_1$, $\mathbf{C}_2$, …, $\mathbf{C}_N$ can be represented by the matrix sums (Olson et al., 2014):

$$\rho(\sigma_N, \boldsymbol{C}_k) = \sum_{j=1}^{N} \sigma_N^{k-1} \otimes \mathbf{C}_k = \mathrm{circ}(\mathbf{C}_1, \mathbf{C}_2, \ldots, \mathbf{C}_N) \tag{8}$$

where $\rho(\,)$, σ_N, and $\otimes$denote the finite sum of the direct products, the N × N cyclic forward-shift matrix, and the Kronecker product, respectively. Using real quasi-equivalent block Fourier matrices (Bladh et al., 2000; Olson et al., 2014), all the matrices can be transformed into pseudo-block diagonal matrices.

The matrices of a single sector established in their own coordinates are consistent, and the displacement of the interface DOFs algorithms with adjacent sectors is shown in Figure 1. The interface DOFs must be described using the same coordinates (Sun et al., 2020). Consequently, the matrices can be transformed as follows.

$$\mathbf{K} = \mathrm{circ}(\mathbf{K}^1, \mathbf{K}^2, \ldots, \mathbf{K}^N), \quad \mathbf{K}^1 = \begin{bmatrix} \mathbf{R}^{\mathrm{T}}\mathbf{k}_{pp}\mathbf{R} + \mathbf{k}_{tt} & \mathbf{k}_{t\bar{g}} \\ \mathbf{k}_{\bar{g}t} & \mathbf{k}_{\bar{g}\bar{g}} \end{bmatrix}, \quad \mathbf{K}^2 = \begin{bmatrix} \mathbf{k}_{tp}\mathbf{R} & \mathbf{0} \\ \mathbf{k}_{\bar{g}p}\mathbf{R} & \mathbf{0} \end{bmatrix} \tag{9}$$

$$\mathbf{K}^N = (\mathbf{K}^2)^{\mathrm{T}}, \quad \mathbf{K}^3 = \mathbf{K}^4 = \cdots = \mathbf{K}^{N-1} = \mathbf{0} \tag{10}$$

where, $\mathbf{R}$ is a linear transformation matrix. Thus, the dynamic model of the entire system can be written as:

$$\mathbf{M}\ddot{\mathbf{u}} + \mathbf{C}\dot{\mathbf{u}} + \mathbf{K}\mathbf{u} = \mathbf{F} \tag{11}$$

The obtained block circulant matrix can be pseudo-diagonalised using the real quasi-equivalent block Fourier matrices $\mathscr{F}$, considering the sector angle $\alpha = 2\pi/N$ (Olson et al., 2014):

$$\mathbf{U} = [\mathbf{u}^1 \quad \mathbf{u}^2 \quad \cdots \quad \mathbf{u}^N] = \mathscr{F}[\mathbf{x}^0 \quad \mathbf{x}_c^1 \quad \mathbf{x}_s^1 \quad \cdots \quad \mathbf{x}^{N/2}] = \mathscr{F}\mathbf{X} \tag{12}$$

$$\mathscr{F} = \left[\mathscr{F}_0 \quad \cdots \quad \mathscr{F}_{N,c} \quad \mathscr{F}_{N,s} \quad \cdots \quad \mathscr{F}_{\frac{N}{2}}\right] \otimes \boldsymbol{I}_k = \frac{1}{\sqrt{N}} \begin{bmatrix} 1 & \sqrt{2} & 0 & \cdots & 1 \\ 1 & \sqrt{2}\cos\alpha & \sqrt{2}\sin\alpha & \cdots & -1 \\ 1 & \sqrt{2}\cos 2\alpha & \sqrt{2}\sin 2\alpha & \cdots & -1 \\ \vdots & \vdots & \vdots & \ddots & \vdots \\ 1 & \sqrt{2}\cos(N-1)\alpha & \sqrt{2}\sin(N-1)\alpha & \cdots & -1 \end{bmatrix} \otimes \boldsymbol{I}_k \tag{13}$$

Substitute (12) into (11) and left multiplicate the transpose of $\mathscr{F}$ to obtain the following.

$$\tilde{\mathbf{M}}\ddot{\mathbf{x}} + \tilde{\mathbf{C}}\dot{\mathbf{x}} + \tilde{\mathbf{K}}\mathbf{x} = \tilde{\mathbf{F}} \tag{14}$$

$$\begin{aligned} \tilde{\mathbf{M}} &= \mathscr{F}^T\mathbf{M}\mathscr{F} = diag(\tilde{\mathbf{M}}^0, \tilde{\mathbf{M}}^1, \cdots, \tilde{\mathbf{M}}^{N/2}), \\ \tilde{\mathbf{C}} &= \mathscr{F}^T\mathbf{C}\mathscr{F} = diag(\tilde{\mathbf{C}}^0, \tilde{\mathbf{C}}^1, \cdots, \tilde{\mathbf{C}}^{N/2}), \\ \tilde{\mathbf{K}} &= \mathscr{F}^T\mathbf{K}\mathscr{F} = diag(\tilde{\mathbf{K}}^0, \tilde{\mathbf{K}}^1, \cdots, \tilde{\mathbf{K}}^{N/2}) \end{aligned} \tag{15}$$

Thus, the total stiffness matrix can be transformed into a pseudo-block matrix, wherein every diagonal element represents one nodal diameter characteristic.

When the damping matrix is ignored, the eigenfrequencies for cyclic symmetric structures under open- and short-circuit can be obtained using the following equations:

$$\left[\widetilde{\mathbf{K}}^r-(\omega^r)^2\widetilde{\mathbf{M}}^r\right]\boldsymbol{\Phi}^r=0,\ \widetilde{\mathbf{K}}^r=\begin{cases}\begin{bmatrix}\widetilde{\mathbf{K}}_{11}^r & \widetilde{\mathbf{K}}_{12}^r\\ \widetilde{\mathbf{K}}_{21}^r & \widetilde{\mathbf{K}}_{22}^r\end{bmatrix}_r, r=1,2,\cdots,\frac{N}{2}-1\\ \widetilde{\mathbf{K}}^0 \text{ or } \widetilde{\mathbf{K}}^{N/2}, r=0 \text{ or } \frac{N}{2}\end{cases} \tag{16}$$

where r denotes the harmonic order. Henceforth, the structural matrices $\widetilde{\mathbf{M}}^r$ and $\widetilde{\mathbf{C}}^r$ have the same form as the stiffness matrix $\widetilde{\mathbf{K}}^r$ in (16).

Considering the presence of a damping matrix within a system, the complex mode superposition method is highly effective for calculating the vibration response (Rao, 2019). Because the dynamic matrices of the entire system are decoupled, the equation of motion in wavenumber space is written as

$$\widetilde{\mathbf{M}}^r\ddot{\mathbf{X}}^r+\widetilde{\mathbf{C}}^r\dot{\mathbf{X}}^r+\widetilde{\mathbf{K}}^r\mathbf{X}^r=\widetilde{\mathbf{F}}^r \tag{17}$$

The characteristic equation of complex mode is given by

$$\mathbf{A}^r\dot{\bar{\mathbf{X}}}+\mathbf{B}^r\bar{\mathbf{X}}=\mathbf{0} \tag{18}$$

$$\mathbf{A}^r=\begin{bmatrix}\widetilde{\mathbf{C}}^r & \widetilde{\mathbf{M}}^r\\ \widetilde{\mathbf{M}}^r & \mathbf{0}\end{bmatrix},\quad \mathbf{B}^r=\begin{bmatrix}\widetilde{\mathbf{K}}^r & \\ & \widetilde{\mathbf{M}}^r\end{bmatrix},\quad \bar{\mathbf{X}}^r=\begin{bmatrix}\boldsymbol{\Psi}^r\\ \boldsymbol{\Psi}^r\lambda^r\end{bmatrix}e^{\lambda t} \tag{19}$$

Supposing $a_k^r=(\bar{\boldsymbol{\Psi}}_k^r)^T\mathbf{A}_k^r\bar{\boldsymbol{\Psi}}_k^r$, the transfer function can be written as

$$\mathbf{H}^r(\omega)=\sum_{k=1}^{N}\left[\frac{\bar{\boldsymbol{\Psi}}_k^r(\bar{\boldsymbol{\Psi}}_k^r)^T}{a_k^r(j\omega-\lambda_k^r)}+\frac{\bar{\boldsymbol{\Psi}}_k^{r*}(\bar{\boldsymbol{\Psi}}_k^{r*})^T}{a_k^{r*}(j\omega-\lambda_k^r)}\right] \tag{20}$$

The response of every nodal diameter can be written as:

$$\mathbf{X}^r=[\mathbf{X}_c^r\quad \mathbf{X}_s^r]^T=\mathbf{H}^r(\omega)\widetilde{\mathbf{F}}^r \tag{21}$$

Using (12), the total response of the cyclic symmetric structure with a piezoelectric vibration absorber can be obtained. The algorithm pseudo-code for vibration response of the CSEM is shown in Algorithm 1.

Algorithm 1: Vibration response of the cyclic symmetric electromechanical model

Input:

- geometrical and mechanical properties of one sector in the cyclic symmetric structure and the piezoelectric patch
- the total number of the sectors N and the position of piezoelectric patch x_p
- the circuit parameters L, R, C_{neg}

Initialization

calculate the matrices and vectors of the CSEM ($\mathscr{F}, \tilde{\mathbf{M}}_r, \tilde{\mathbf{C}}_r, \tilde{\mathbf{K}}_r, \tilde{\mathbf{F}}_r$);

calculate ω_{sc} and ω_{oc};

for $\omega = \omega_s : \omega_e$ **do**

  for r = 1:N/2+1 **do**

    $a^r = 0$;

    if $\omega_{sc}(i) < 2\omega_e$ **then** $a_i^r = \bar{\boldsymbol{\Psi}}_i^{rT} \mathbf{A}_i^r \bar{\boldsymbol{\Psi}}_i^r$; **end**

    $a^r = \text{sum}(a_i^r)$; update the transfer function $\mathbf{H}^r$;

    computation of dynamic equation $\mathbf{X}^r = [\mathbf{X}_c^r \quad \mathbf{X}_s^r]^T = \mathbf{H}^r \mathbf{F}^r$;

    wave number increment;

  end

  update the total response **U** of the CSEM;

  frequency increment;

end

Output:

- eigenfrequencies and the modal shape
- vibration responses of coupling system ($\boldsymbol{u}, \dot{\boldsymbol{u}}, \ddot{\boldsymbol{u}}$)

3. Validation of theoretical analysis by simulations and experiments

In this section, the vibration characteristics of the proposed CSEM are compared with those of the FEM without cyclic reduction and with the experimental results for validation. First, an experimental test rig for electromechanical coupling system vibration was established. As shown in Figure 3, a simplified blisk equipped with a piezoelectric vibration absorber was used as an example. Based on this system, natural frequency comparisons between the CSEM, entire FEM, and experiment were carried out. To assess the vibration control effect, the performance of PVA with various shunt circuits were numerically evaluated and compared.

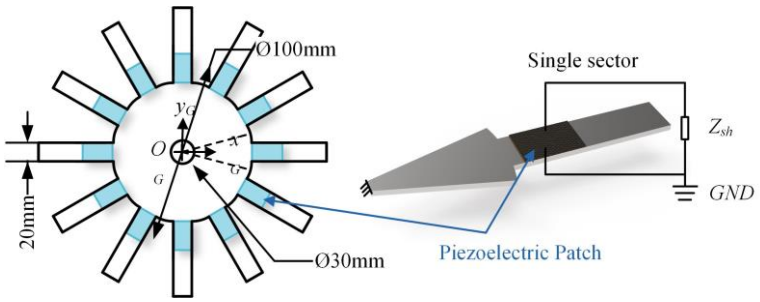

Figure 3. Schematic of the simplified blisk with piezoelectric vibration absorber.

3.1. Experimental set-up

As shown in Figure 3, a piezoelectric patch was attached to each sector in the blisk. The material of the blisk was AL6061 and the elastic modulus, density and Passion's ratio was E = 69 GPa, ρ_b = 2750 Kg/m^3 and υ = 0.33, respectively. The thickness of the blisk and length of the blade were t_b = 3 mm and l_b = 70 mm. MFC (M2814) was selected as the piezoelectric transducer, and elastic, piezoelectric, and permittivity constants were c_{11} = 69.48 GPa, c_{12} = 24.32 Gpa, c_{66} = 22.57 GPa, e_{31} = -16.04 C/m^2, and ε_{33}

= 9.56×10^{-9} nF/m, respectively. The length, width, and thickness of the selected piezoelectric patch are chosen as l_p = 28 mm, w_p = 14 mm, t_p = 0.3 mm, respectively.

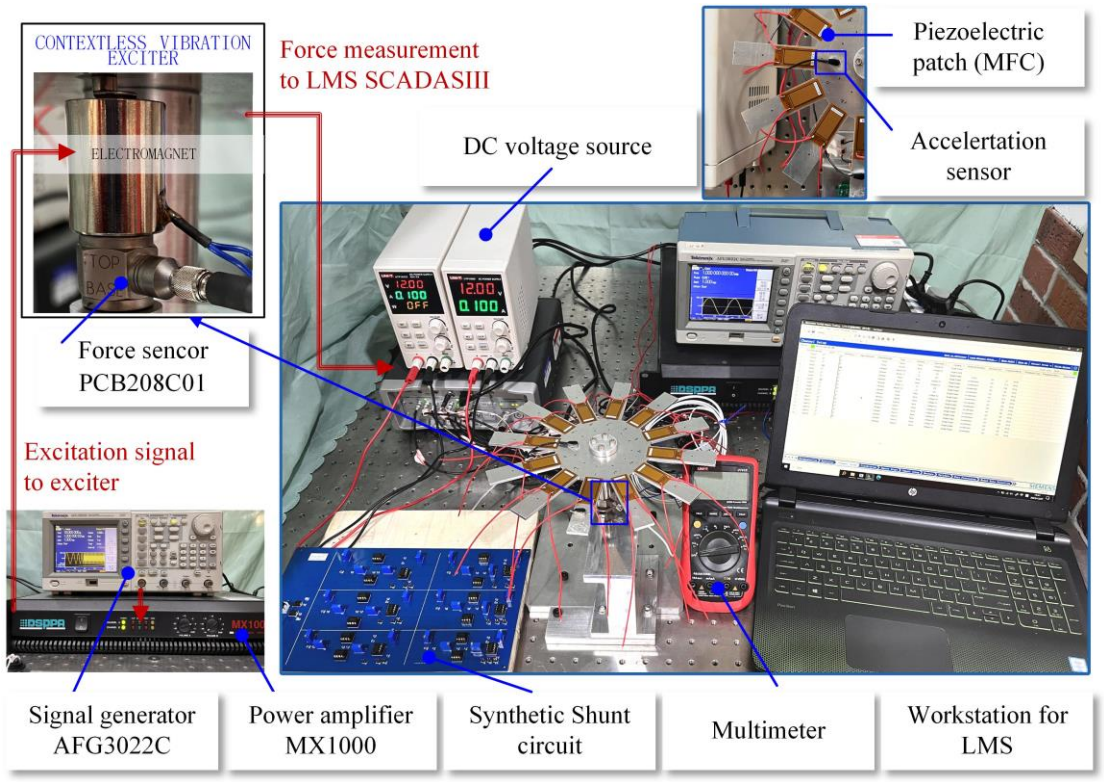

Figure 4. Test rig for the electromechanical coupling system in vibration control.

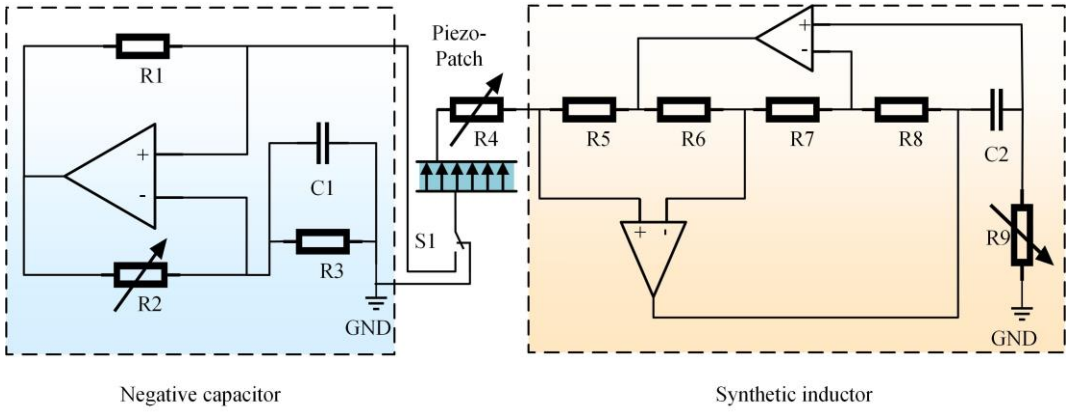

Figure 5. Modified synthetic circuit composing synthetic inductor and negative capacitor (Wangenheim, 1996; Zhou and Hu, 2023).

A test rig for coupling the system vibrations was set up as shown in Figure 4. Subsequently, a blisk was fixed to the platform through the inner hole, and piezoelectric patches were glued to the structure at the end of the sectors. Two accelerometers (YZW-A17C01) were used to measure the system response. Furthermore, an additional force hammer (KISTLER 9724A5000) was used in the hammering test. In the vibration test, an electromagnetic coil was used as the contactless vibration exciter, and a force sensor (PCB 208C01) was used to monitor the magnitude of the excitation force. Additionally, a distributed data acquisition system (LMS, SCADASIII) was employed to collect the dynamic response and output excitation signals.

The PVA used in this study comprised an MFC piezoelectric patch and a synthetic circuit. A piezoelectric patch was glued to the end of each sector. The synthetic circuit comprised a synthetic inductor (Wangenheim, 1996) and a negative capacitor (Zhou and Hu, 2023) as shown in Figure 5. The equivalent inductance, negative capacitance, and resistance were calculated using the following equations:

$$L_{eq} = \frac{C_2 R_8 R_5}{R_6} R_9, \quad R_{eq} = R_4 - \frac{R_5}{R_6} R_7, \quad C_{neg} = -\frac{R_2}{R_1} C_1 \tag{22}$$

A transfer switch 'S1' was used to change the circuit form between the series RL and RLNC circuits. As shown in Figure 5, R2, R4, and R9 were set as potentiometers to adjust the values of the series resistance (R), inductance (L), and NC (C_{neg}).

3.2. Verification of natural characteristic

An FEM without cyclic reduction of a blisk was integrated with a piezoelectric vibration absorber. Solid elements (SOLID45 and SOLID5for the host structure and piezoelectric patches, respectively) were used to simulate the coupling system. The entire FE model was simulated using COMSOL Multiphysics, wherein the upper and lower surfaces of the piezoelectric patches were arranged as electrodes (Sun et al., 2020). A total of 13983 elements were identified. The roving hammer method was employed for modal tests. Two accelerometers were fixed at specific locations on the blisk, and excitations were applied at 67 points across the structure using an impact hammer, excluding the accelerometer positions, and targeting six specific points on one sector of the blisk. At each impact location, the structural response was recorded using accelerometers and the corresponding frequency response functions were calculated.

Table 1 Comparison of natural frequencies of blisk with PVA obtained by entire model, CSEM and experiments.

Order	CSEM (Hz)	FEM (Hz)	Experiment (Hz)	Error 1 (%)	Error 2 (%)
f_1	227.92	228.50	214.45	0.25%	5.90%
f_2	227.92	228.55	217.16	0.28%	4.72%
f_3	240.47	239.96	248.35	0.21%	3.28%
f_4	262.15	261.76	257.57	0.15%	1.75%
f_5	262.15	261.76	258.34	0.15%	1.45%

The resulting natural frequencies of the system obtained through the FEM, CSEM, and experimental tests are listed in Table 1. The findings revealed that the CSEM results aligned closely with the experimental results, with the maximum deviation of the first five undamped natural frequencies of the blisk between the CSEM and experimental results being less than 5%, except for the first-order frequency (note that these frequencies pertain to undamped conditions). However, Error 1 was smaller than Error 2, indicating that the CSEM results more closely resembled the FEM results than the experimental findings. Notably, potential factors such as minor mistuning during the blisk and piezoelectric patch manufacturing processes and inconsistencies in the applied hammering force during the experiment, could have impacted these results. Error 2 of the first order was likely caused by the influence of the accelerometers on the blade.

The resulting natural frequencies of the system obtained through entire FEM, CSEM, and experimental tests, are provided in Table 1. The findings reveal that the CSEM results align closely with

the experimental results, with the maximum deviation of the first five undamped natural frequencies of the blisk between the CSEM and experimental results being less than 5% except the first order (It is important to note that these frequencies pertain to undamped conditions). However, Error 1 is smaller than Error 2, indicating that the CSEM results exhibit a closer resemblance to the FEM results compared to the experimental findings. It is worth mentioning that potential factors such as minor mistuning during the blisk and piezoelectric patch manufacturing process, as well as inconsistencies in the applied hammering force during the experiment, could contribute to these results. And the Error 2 in the first order may be caused by the influence of the accelerometers in the blade.

3.3. Circuit parameters identification

In this experiment, a shunt circuit was constructed using a synthetic circuit, making direct measurements impracticable. Consequently, an indirect measurement method was employed to determine the synthetic inductance and negative capacitance. As shown in Figure 6, the synthetic inductor is connected in series with an auxiliary resistor R_c = 10^4 Ω, with an AC signal of varying frequency generated by a signal generator. The voltage across the inductor v_L and the output voltage v from the signal generator were measured using an LMS system, and their frequency response functions (FRFs) are:

$$\frac{v}{v_L} = -j\frac{R_c}{\omega L} + 1 \tag{23}$$

Considering the reciprocal of the imaginary part, the slope of the curve is denoted by s_L, and the inductance can be calculated using $L = s_L R_c$. The inductance results of the RL and RLNC circuits are shown in Figure 6(a). The inductance values calculated from the slopes are 14.84 and 3.64 H in RL and RLNC circuit, respectively. The identification process of C_{neg} is similar to that of the synthetic inductance, as shown in Figure 6(b). Furthermore, C_{neg} is calculated to be 38.58 nF.

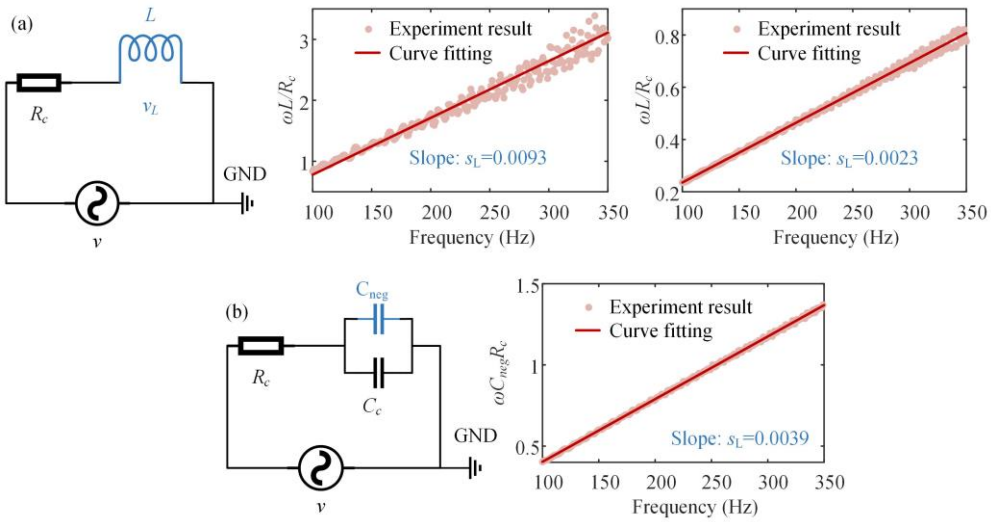

Figure 6. identification of circuit parameters: (a) Synthetic inductance; (b) NC.

3.4. Verification of vibration response with different circuit designs

To further validate the accuracy of the CSEM, the vibration responses were compared with those obtained from the FEM and the experimental results. As listed in Table 2, three distinct scenarios were

examined: PVA with short circuits, RL shunt circuits, and RLNC shunt circuits. In the simulation, Rayleigh damping was employed, with $\alpha = 7.3522$ and $\beta = 3.3979\times 10^{-6}$. The frequency step was set to 0.5 Hz, and an external force amplitude of 0.005 N was applied, corresponding to parameters derived from the calibration experiments utilising a non-contact excitation system.

Table 2 External electric boundary types and specific values in different cases.

Case	External electric boundary types	Values
Case 1	Short circuit	Without control
Case 2	RL resonant circuit	R = 14300 Ω, L= 14.84 H
Case 3	RLNC circuit	R = 7295 Ω, L = 3.64 H, C_{neg} = 38.58 nF

As shown in Figure 7, the results obtained by the CSEM and FEM exhibit a high degree of agreement, numerically validating the proposed model. In this study, vibration mode f_3 (240.47 Hz) in Table 1 is considered the targeted mode to be controlled because it has the same shape for each sector, and the same method can be extended to other modes. The vibration responses around the target mode obtained by the CSEM and FEM were compared to investigate the applicability of the proposed model under different electrical boundaries. The frequency step was set to 0.1 Hz, and the results are shown in Figure 7. The results based on the CSEM agreed with those based on the FEM.

The comparison results with the experimental results presented in Figure 8 indicate the efficacy of PVA in attenuating the vibration amplitude of the blisk. Notably, the vibration response decreased substantially with the incorporation of the shunt circuit. The simulated results show a 54.9% and 66.3% reduction in the vibration response in the RL and RLCN shunt circuits, respectively. The experimental data corroborate these findings, with an observed decrease of 28.5% and 35.4% for the RL and RLNC shunt circuits, respectively.

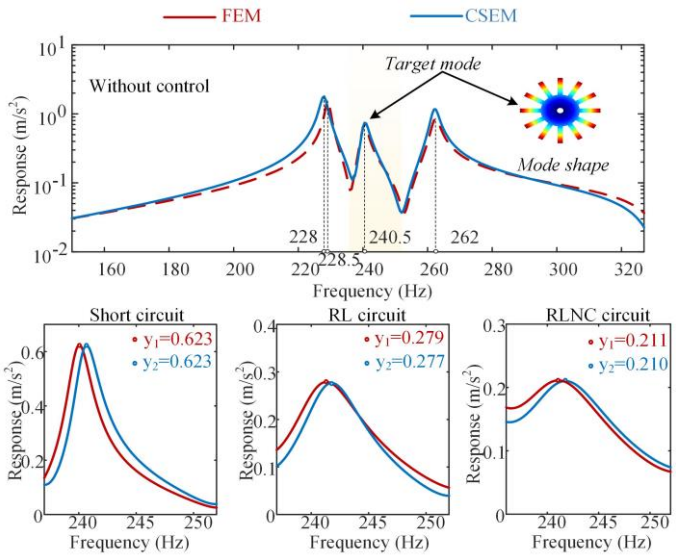

Figure 7. Vibration response comparison between FEM and CSEM under different shunt circuits.

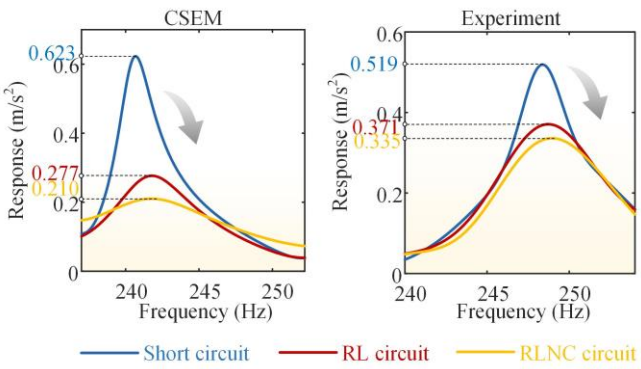

Figure 8. Vibration control effect of PVA connected with different shunt circuits.

4. Further parametric analysis

Based on the proposed CSEM established in Section 2, the parameter analysis consisted of two parts to study the vibration control effect of the PVA: the effect of circuit parameters, including the inductance and NC, and the positioning of the piezoelectric patches on the blades. The vibration suppression effect was used to quantify the performance of the PVA (Pourkiaee et al., 2022):

$$\text{The suppression effect of PVA} \Rightarrow \frac{\text{Reduction of Peak}}{\text{The peak of open circuit state}} \times 100\% \tag{24}$$

4.1. The effect of circuit parameters L and C_{neg}

A previously established CSEM was utilised to analyse the effects of L and C_{neg} on the vibration control of the blisk, with parameters corresponding to those detailed in Section 3. For RL shunt circuits, attention is focused primarily on circuit detuning resulting from variations in the inductance parameters. The resistance is maintained at 14300 Ω, while the inductance varies from 5 H to 45 H. The vibration response of the target mode before and after the implementation of the PVA is shown in Figure 9. For the current system, the optimal inductance was 15 H, which coincides with the value calculated using Equation (A.1). Figure 9 also illustrates that the PVA achieves a maximum suppression effect of 54.9%, beyond which the performance deteriorates notably owing to circuit detuning, particularly when the inductance exceeds 25 H.

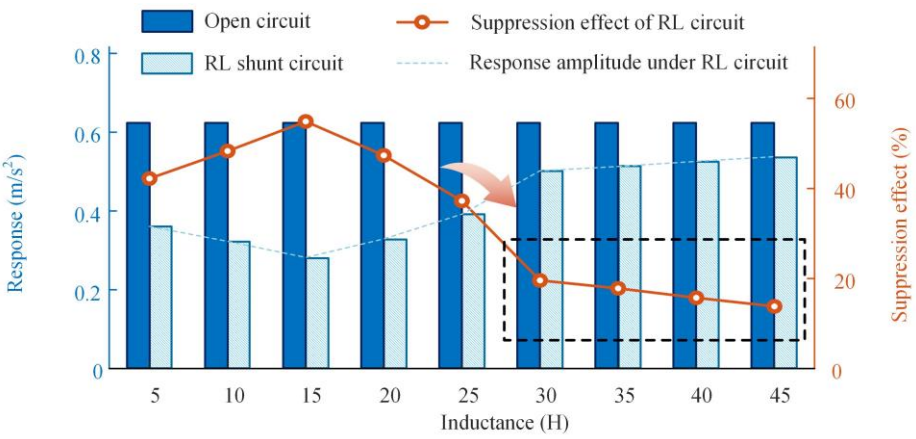

Figure 9. Vibration control performance of PVA with different inductance.

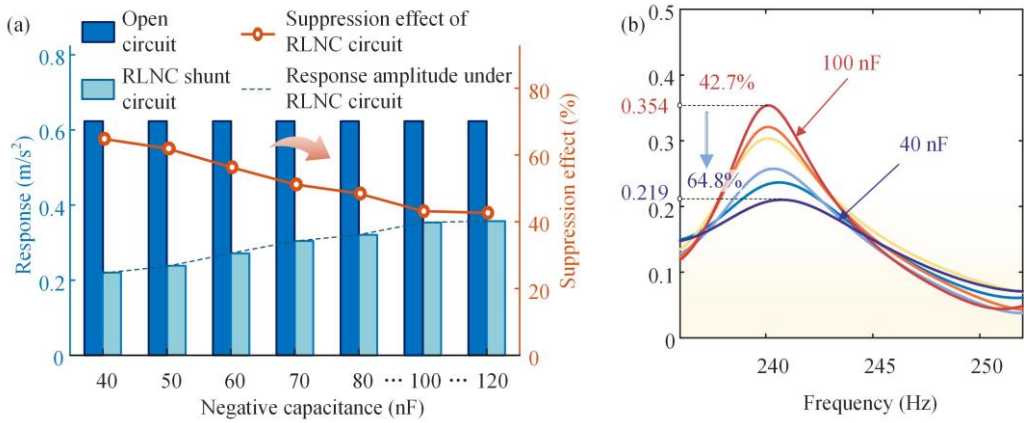

Figure 10. Vibration response of blisk calculated by CSEM: (a) Vibration control performance of PVA with different NC; (b) vibration responses variations with NC.

For the RLNC shunt circuit, the value of the NC is investigated. Considering the stability of PVA, the absolute value of NC must be greater than the inherent capacitance of the piezoelectric patch (Berardengo et al., 2016). In this study, the NC is set from -40 nF to -120 nF and the other parameters are the same as those in Section 3. Consistent with the parameter analysis of the inductor, the response amplitude of the target mode with and without control, as calculated by CSEM, is shown in Figure 10. According to the calculations, the vibration response with control increased with an increase in the absolute value of NC. The best performance of the PVA with a series RLNC circuit was observed at NC = 40 nF, with a suppression effect of 64.8%. This demonstrates that, provided the system remains stable, an increase in NC in the external circuit cancelling the inherent capacitance of the piezoelectric patch, enhances the vibration control performance.

Comparing the results depicted in Figure 9, the suppression effect is close to that of the series RL circuit with an increase in the absolute value of NC (especially when it is greater than 80 nF). This makes NC less effective in cancelling the inherent capacitance of the piezoelectric patch.

4.2. Effect of piezoelectric patch placement

Based on the CSEM image of the blisk with PVA, the effect of the position of the piezoelectric patch on the vibration suppression effect of PVA was analysed. The position of the piezoelectric patch was denoted by its distance from the blade root. The distance was set from 0–40 mm, and the other parameters were the same as those described in Section 3. The response results calculated by the CSEM are shown in Figure 11. The PVA evidently exhibits vibration suppression effect when arranged in different positions. For both the RL and RLNC circuits, the closer the blade roots, the better the vibration control performance.

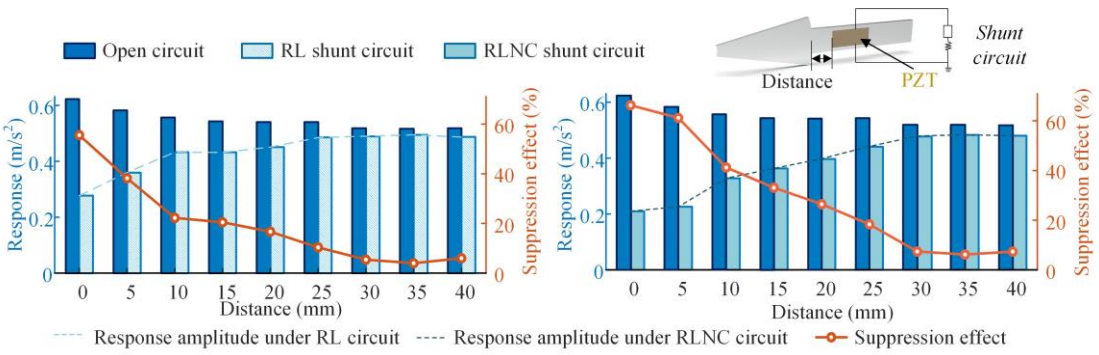

Figure 11. Vibration response and suppression effect of blisk with PVA calculated by CSEM.

To examine into the underlying reasons for the effect of piezoelectric patch placement on vibration suppression, the modal electromechanical coupling factor (MEMCF) was calculated based on the CSEM in this study, as shown in Figure 12. The suppression performance of the PVA under different circuits changes with the placement variation, as illustrated in Figure 12.

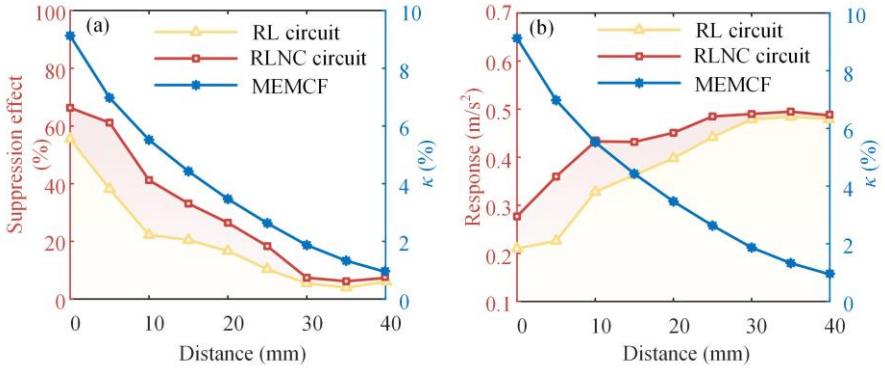

Figure 12. Changes in MEMCF and vibration suppression effect with the variation of piezoelectric patch placement: (a) Suppression effect; (b) Vibration response.

MEMCF serves as a reliable measure of the energy transformation capability of piezoelectric transducers. For the controlled mode, the calculations indicate that positioning the piezoelectric patch closer to the blade root increases the MEMCF and enhances the vibration control effect. In other words, the vibration control performance is positively related to the ability of the piezoelectric transducer to convert electrical energy. Moreover, the results indicate that the enhancement effect of NC on the vibration reduction performance of PVA is weakened with the decrease in MEMCF.

5. Conclusions

This study presented a novel and comprehensive CSEM for evaluating the vibration characteristics of structures with PVA. The integration of the complex mode superposition method with the CSEM offers a robust approach for analysing dynamic responses. Numerical simulations and experimental results validate the accuracy and effectiveness of the proposed model. The analysis focused on a simplified blisk equipped with PVA to investigate the effects of the synthetic circuit parameters and the placement of piezoelectric transducers on the effectiveness of vibration control. The main conclusions drawn from this study are as follows:

(1) A novel CSEM integrated with PVAs was proposed based on circulant matrix theory. The vibration characteristics derived from this model aligned closely with the results obtained through the FEM and experimental findings, thus validating the model's efficacy.

(2) A synthetic circuit consisting of a negative capacitor was utilised in the PVAs for vibration control of the simplified blisk. The suppression effect for the target mode was 28.5% and 35.4% for the RL and RLNC shunt circuits, respectively.

(3) Parameter analysis indicated that the optimal inductance is coincided with the analytical value. Additionally, the optimal value for NC was slightly larger than the inherent capacitance the piezoelectric transducer for both the RL and RLNC circuit, positioning the piezoelectric patch closer to the blade root improved the vibration control.

Acknowledgements

The authors gratefully acknowledge the support provided by the National Natural Science Foundation of China (NSFC, Grant No. 51975354 and 52211530093) and the support from Royal Society (Grant No. IEC\NSFC\211005). We also would like to thank Editage (www.editage.com) for English language editing.

Statements and Declarations

The author(s) declared no potential conflicts of interest with respect to the research, authorship, and/or publication of this article.

Appendix

The optimal values of R and L in the series RL shunt circuit (as shown in Figure 2(a)) can be obtained using the following equations (Thomas et al., 2009; Yamada et al., 2010):

$$L_s^{opt} = \frac{1}{(1+\kappa^2)\omega_{sc}^2 C_{pe}}, \quad R_s^{opt} = \sqrt{\frac{3\kappa^2}{(1+\kappa^2)(2+\kappa^2)}}\frac{1}{\omega_{sc}C_{pe}} \tag{A.1}$$

$$\kappa = \sqrt{(\omega_{oc}^2 - \omega_{sc}^2)/\omega_{sc}^2} \tag{A.2}$$

where ω_{sc} and ω_{oc} are the eigenfrequencies of the short and open circuits, respectively. And κ denotes the modal electromechanical coupling factor (MEMCF).

When the NC is connected to the series RL circuit (as shown in Figure 2(b)), the optimal parameters for the RLNC circuit is given by (Berardengo et al., 2021; Thomas et al., 2009; Yamada et al., 2010):

$$L_{s,NC}^{opt} = \frac{\alpha}{(1+\alpha)(1+\kappa^2)\omega_{sc}^2 C_{pe}}, \quad R_{s,NC}^{opt} = \sqrt{\frac{3\alpha^2\kappa^2}{(1+\alpha)(1+\kappa^2)(\alpha\kappa^2-\kappa^2+2\alpha)}}\frac{1}{\omega_{sc}C_{pe}} \tag{A.3}$$

It is assumed that $C_{neg} = -(1+\alpha)C_{pe}$ and the NC must be higher than the inherent capacitance of the piezoelectric patch C_{pe} for stability condition (Berardengo et al., 2016).

Reference

Alfahmi O and Erturk A (2024) Programmable hardening and softening cubic inductive shunts for piezoelectric structures: Harmonic balance analysis and experiments. *Journal of Sound and Vibration* 571: 118029.

Anusonti-Inthra P and Gandhi F (2000) Helicopter Vibration Reduction through Cyclic Variations in Rotor Blade Root Stiffness. *Journal of Intelligent Material Systems and Structures* 11(2): 153–166.

Berardengo M, Thomas O, Giraud-Audine C, et al. (2016) Improved resistive shunt by means of negative capacitance: new circuit, performances and multi-mode control. *Smart Materials and Structures* 25(7): 075033.

Berardengo M, Høgsberg J, Manzoni S, et al. (2020) LRLC-shunted piezoelectric vibration absorber. *Journal of Sound and Vibration* 474: 115268.

Berardengo M, Manzoni S, Thomas O, et al. (2021) Guidelines for the layout and tuning of piezoelectric resonant shunt with negative capacitances in terms of dynamic compliance, mobility and accelerance. *Journal of Intelligent Material Systems and Structures* 32(17): 2092–2107.

Bladh R, Castanier MP and Pierre C (2000) Component-Mode-Based Reduced Order Modeling Techniques for Mistuned Bladed Disks—Part I: Theoretical Models. *Journal of Engineering for Gas Turbines and Power* 123(1): 89–99.

Cross CJ and Fleeter S (2002) Shunted piezoelectrics for passive control of turbomachine blading flow-induced vibrations. *Smart Materials and Structures* 11(2): 239.

Dai S, Zheng Y, Mao J, et al. (2023) Vibro-acoustic control of a programmable meta-shell with digital piezoelectric shunting. *International Journal of Mechanical Sciences* 255: 108475.

Ewins DJ (1973) Vibration Characteristics of Bladed Disc Assemblies. *Journal of Mechanical Engineering Science* 15(3): 165–186.

Ewins DJ (2010) Control of vibration and resonance in aero engines and rotating machinery – An overview. *International Journal of Pressure Vessels and Piping* 87(9). Dynamic Loading of Components and Structures: 504–510.

Fleming AJ, Behrens S and Moheimani SOR (2000) Synthetic impedance for implementation of piezoelectric shunt-damping circuits. *Electronics Letters* 36(18): 1525.

Gripp JAB and Rade DA (2018) Vibration and noise control using shunted piezoelectric transducers: A review. *Mechanical Systems and Signal Processing* 112: 359–383.

Jamshidi R and Jafari AA (2022) Nonlinear vibration of conical shell with a piezoelectric sensor patch and a piezoelectric actuator patch. *Journal of Vibration and Control* 28(11–12): 1502–1519.

Liu J, Li L, Huang X, et al. (2017) Dynamic characteristics of the blisk with synchronized switch damping based on negative capacitor. *Mechanical Systems and Signal Processing* 95: 425–445.

Luo A, Lossouarn B and Erturk A (2024) Multimodal vibration damping of a three-dimensional circular ring coupled to analogous piezoelectric networks. *Journal of Sound and Vibration* 581: 118385.

Mosquera-Sánchez JA, Alfahmi O, Erturk A, et al. (2024) Broadening the frequency response of a Duffing-type piezoelectric shunt by means of negative capacitance. *Journal of Sound and Vibration* 578: 118344.

Neubauer M, Oleskiewicz R, Popp K, et al. (2006) Optimization of damping and absorbing performance of shunted piezo elements utilizing negative capacitance. *Journal of Sound and Vibration* 298(1): 84–107.

Olson BJ, Shaw SW, Shi C, et al. (2014) Circulant Matrices and Their Application to Vibration Analysis. *Applied Mechanics Reviews* 66(4): 040803.

Petrov EP (2004) A Method for Use of Cyclic Symmetry Properties in Analysis of Nonlinear Multiharmonic Vibrations of Bladed Disks. *Journal of Turbomachinery* 126(1): 175–183.

Pohl M and Rose M (2016) Piezoelectric shunt damping of a circular saw blade with autonomous power supply for noise and vibration reduction. *Journal of Sound and Vibration* 361: 20–31.

Pourkiaee SM, Zucca S and Parker RG (2022) Relative cyclic component mode synthesis: A reduced order modeling approach for mistuned bladed disks with friction interfaces. *Mechanical Systems and Signal Processing* 163: 108197.

Qi R, Wang L, Jin J, et al. (2023) Enhanced Semi-active piezoelectric vibration control method with shunt circuit by energy dissipations switching. *Mechanical Systems and Signal Processing* 201: 110671.

Rao SS (2019) *Vibration of Continuous Systems*. John Wiley & Sons.

Richardt JD, Lossouarn B, Høgsberg J, et al. (2024) Calibration of multiple shunted piezoelectric transducers with correction for residual modes and shunt interactions. *Journal of Vibration and Control*: 10775463241241838.

Shen J, Sun W and Xu K (2023) Semi-analytical dynamic modeling and vibration reduction analysis of the blisk structure with piezoelectric shunt damping patches. *Applied Acoustics* 211: 109502.

Shevtsov S, Soloviev A, Acopyan V, et al. (2009) Helicopter Rotor Blade Vibration Control on the Basis of Active/Passive Piezoelectric Damping Approach. Epub ahead of print 2009.

Soltani P, Kerschen G, Tondreau G, et al. (2014) Piezoelectric vibration damping using resonant shunt circuits: an exact solution. *Smart Materials and Structures* 23(12): 125014.

Sun W, Yang S, Gao J, et al. (2020) A cyclic symmetric model for the investigation of vibration reduction of hard-coating blisk. *Engineering Computations* 37(9). Emerald Publishing Limited: 3387–3406.

Sun Y, Yuan J, Denimal E, et al. (2021) Nonlinear Modal Analysis of Frictional Ring Damper for Compressor Blisk. *Journal of Engineering for Gas Turbines and Power* 143(3): 031008.

Tang J and Wang KW (2003) Vibration Delocalization of Nearly Periodic Structures Using Coupled Piezoelectric Networks. *Journal of Vibration and Acoustics* 125(1): 95–108.

Thomas O, Deü J-F and Ducarne J (2009) Vibrations of an elastic structure with shunted piezoelectric patches: efficient finite element formulation and electromechanical coupling coefficients. *International Journal for Numerical Methods in Engineering* 80(2): 235–268.

Wangenheim L von (1996) Modification of the classical GIC structure and its application to RC-oscillators. *Electronics Letters* 32(1). IET Digital Library: 6–8.

Yamada K, Matsuhisa H, Utsuno H, et al. (2010) Optimum tuning of series and parallel LR circuits for passive vibration suppression using piezoelectric elements. *Journal of Sound and Vibration* 329(24): 5036–5057.

Yang J, Beirow B and Giersch T (2022) Simulation and Investigation of an Intentionally Mistuned Blisk Rotor in a High Pressure Compressor. In: *ASME Turbo Expo 2022: Turbomachinery Technical Conference and Exposition*, 28 October 2022. American Society of Mechanical Engineers Digital Collection. Available at: https://dx.doi.org/10.1115/GT2022-82576 (accessed 28 January 2024).

Yuan J, Scarpa F, Allegri G, et al. (2017) Efficient computational techniques for mistuning analysis of bladed discs: A review. *Mechanical Systems and Signal Processing* 87: 71–90.

Zhou B, Thouverez F and Lenoir D (2014) Vibration Reduction of Mistuned Bladed Disks by Passive Piezoelectric Shunt Damping Techniques. *AIAA Journal* 52(6): 1194–1206.

Zhou K and Hu Z (2023) Vibration Suppression on the Composite Laminated Plates Subjected to Aerodynamic and Harmonic Excitations Based on the Nonlinear Piezoelectric Shunt Damping. *Applied Mathematical Modelling* 121: 134–165.

Zhou K, Hu Z and Hua H (2021) Investigation of the Nonstationary Stochastic Response of Functionally Graded Piezoelectric Material Plates with General Boundary Conditions. *Applied Mathematical Modelling* 96: 315–335.